ACS APPLIED MATERIALS & INTERFACES

Research Article

www.acsami.org

Investigation of Photovoltaic Properties of Single Core–Shell GaN/InGaN Wires

A. Messanvi,[*,†,‡,§] H. Zhang,[†] V. Neplokh,[†] F. H. Julien,[†] F. Bayle,[†] M. Foldyna,[∥] C. Bougerol,[‡,⊥] E. Gautier,[‡,#] A. Babichev,[¶] C. Durand,[‡,§] J. Eymery,[‡,§] and M. Tchernycheva[*,†]

[†]Institut d'Electronique Fondamentale, UMR CNRS 8622, University Paris Sud 11, 91405 Orsay, France

[‡]Université Grenoble Alpes, 38000 Grenoble, France

[§]CEA, INAC-SP2M, "Nanophysique et semiconducteurs" group, 38000 Grenoble, France

[∥]LPICM, Ecole Polytechnique, CNRS, 91128 Palaiseau, France

[⊥]CNRS, Inst. NEEL, 38042 Grenoble, France

[#]CEA, INAC-SPINTEC, 38000 Grenoble, France

[¶]ITMO University, 197101 St. Petersburg, Russia

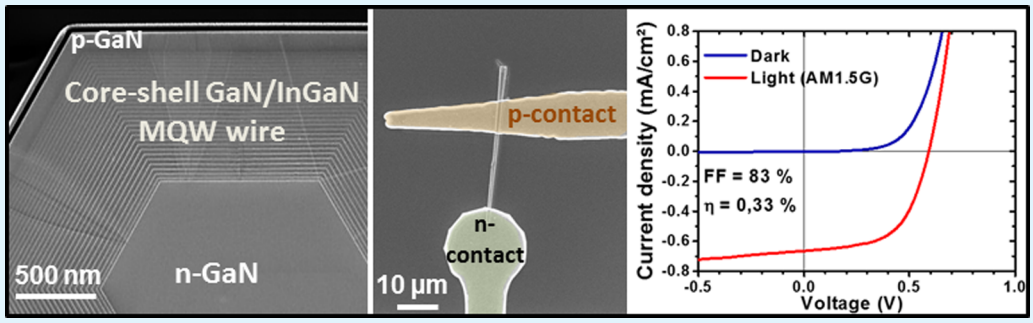

ABSTRACT: We report the investigation of the photovoltaic properties of core–shell GaN/InGaN wires. The radial structure is grown on m-plane $\{1\bar{1}00\}$ facets of self-assembled $\bar{c}$-axis GaN wires elaborated by metal–organic vapor phase epitaxy (MOVPE) on sapphire substrates. The conversion efficiency of wires with radial shell composed of thick $In_{0.1}Ga_{0.9}N$ layers and of 30× $In_{0.18}Ga_{0.82}N$/GaN quantum wells are compared. We also investigate the impact of the contact nature and layout on the carrier collection and photovoltaic performances. The contact optimization results in an improved conversion efficiency of 0.33% and a fill factor of 83% under 1 sun (AM1.5G) on single wires with a quantum well-based active region. Photocurrent spectroscopy demonstrates that the response ascribed to the absorption of InGaN/GaN quantum wells appears at wavelengths shorter than 440 nm.

KEYWORDS: *wires, InGaN/GaN MQWs, MOVPE, photovoltaics, photocurrent spectroscopy, EBIC*

1. INTRODUCTION

The III-nitride compounds are nowadays intensively explored for their promising potential to harvest solar energy. This interest stems from the possibility to tune the optical bandgap of InGaN films by varying the indium content to match different wavelengths of the solar spectrum (from near-infrared to near-ultraviolet range).[1] InGaN films are particularly well adapted for the conversion of the blue spectral range of the solar spectrum.[2] This property is relevant for the integration of InGaN-based top cells in multijunction solar cells in order to reduce thermalization losses occurring in low/midbandgap solar cells and to increase the open-circuit voltage (V_{oc}). InGaN materials are especially interesting for concentrated photovoltaics (CPV) systems as they exhibit excellent radiation robustness[3] with photovoltaic operation demonstrated under 300 suns.[4]

To date, the best conversion efficiencies under the full AM1.5G solar spectrum reported for III-nitride solar cells have reached 2–3% on sapphire substrates.[2,5,6] The improvement of these performances is hindered by the difficulty to grow InGaN layers with high indium content on high quality GaN templates. Sapphire is the usual substrate for the growth of GaN templates, and the 16% lattice mismatch induces a high density of dislocation (in the 10^8 cm^{-2} range) that degrades the material quality. Besides, the lattice mismatch between GaN and InN (≈12%) causes lattice strain in InGaN thin films. In thick films or layers with high indium content, the strain is relieved by plastic deformations, which result in misfit dislocations and V-pits formation. To avoid defect formation,

Received: July 17, 2015
Accepted: September 17, 2015
Published: September 17, 2015

DOI: 10.1021/acsami.5b06473
ACS Appl. Mater. Interfaces 2015, 7, 21898–21906

the thickness of the InGaN layer should be kept under a critical thickness of a few nanometers for an indium content in the 15−20% range.[7] This constraint goes against the need for thick layers to maximize light absorption. Moreover, the chemical miscibility gap between InN and GaN does not favor the incorporation of indium and causes segregation issues.[8] The presence of both defects and indium fluctuations has a detrimental impact on the performances of photovoltaic devices. To overcome these difficulties, alternative approaches such as multiple quantum wells (MQWs) have been implemented to limit the thickness of the InGaN insertions while conserving a high indium content in the layers.[2,9] The improved crystalline quality of these structures led to better device performances compared to solar cells integrating a thick InGaN absorption layer.[10]

Another innovative approach relies on the use of GaN wire templates for the growth of InGaN-based heterostructures. GaN wires can indeed be grown free of defects thanks to dislocation bending to the free surfaces.[11,12] For very small diameters, radial heterostructures on GaN wires should in principle also benefit from elastic strain relaxation at the lateral free surfaces, but these conditions are in practice difficult to implement in metal−organic vapor phase epitaxy (MOVPE). In any case, the core−shell geometry with strained layers or MQWs enables one to separately optimize photon absorption and carrier extraction, two key processes of photovoltaic operation. Ultimately, the growth of uniform arrays of GaN wires by selective area growth (SAG)[13,14] will allow one to take advantage of light trapping properties shown by nanowire assemblies.[15,16]

Prototypes of solar cells based on InGaN/GaN nanowires have already been reported. Wierer et al.[17] used GaN nanowires, realized by a top-down approach, as templates for the growth of InGaN/GaN MQWs. The modest conversion efficiency of the device (0.3% under 1 sun AM1.5G) was attributed to the presence of electrical shorting paths. A solar cell based on self-assembled p-i-n GaN nanorods with a 200 nm-InGaN axial insertion was recently reported.[18] The device exhibited a high short-circuit current of 4.6 mA/cm^2 but the performances in terms of V_{oc} (0.22 V) and fill factor (34%) remained below state-of-the-art values for thin films.[19,20] In order to improve the conversion efficiency of such devices, it is important to study and understand the photovoltaic properties at the single wire level. Lieber's group at Harvard has investigated InGaN/GaN coaxial nanowires.[21] The heterostructure consisted of an 80−100 nm-thick InGaN layer grown on the polar $\{000\bar{1}\}$ and semipolar facets $\{1\bar{1}01\}$ of GaN nanowires with a triangular cross section. The highest conversion efficiency reached by these nanowires was 0.19% under 1 sun illumination. Although MQW heterostructures have been reported to increase the conversion efficiency of planar devices, no studies have investigated so far the characteristics of single GaN wires integrating radial (and axial) MQWs. The study of a model case of single nanowires is essential to understand the inherent limitations of the InGaN/GaN technology and to establish an optimized architecture of the active region and of the contact layout.

In this work, we report on the photovoltaic properties of single core−shell GaN/InGaN wires. The radial shell is composed of 30× $In_{0.18}Ga_{0.82}N$/GaN MQWs grown on m-plane $\{1\bar{1}00\}$ facets of $\bar{c}$-axis GaN wires. Their performance is compared to that of wires coated with thick $In_{0.1}Ga_{0.9}N$ layers. In parallel, we investigate the influence of the contact scheme on carrier collection and photovoltaic performances. The electron beam induced current microscopy is used to probe the homogeneity of the carrier collection over the core/shell region. The contact optimization results in a conversion efficiency of 0.33% and a fill factor of 83% under 1 sun (AM1.5G) illumination on single InGaN/GaN MQW wires.

2. EXPERIMENTAL METHODS

2.1. Growth of GaN/InGaN Wires. Core−shell GaN/InGaN wires were grown on c-sapphire substrates by MOVPE in a closed coupled showerhead (CSS) reactor. The method employed for the wire growth is described in ref 22. First, the sapphire surface is baked at 1080 °C and nitridated under ammonia (NH_3) flux to form a thin AlN layer that will promote the growth of N-polar wires with m-plane $\{1\bar{1}00\}$ lateral facets. Then, a thin SiN_x layer (~2 nm) is deposited. This SiN layer acts as a mask for the subsequent growth of the GaN wires. After a nucleation step, the growth of a highly doped n-type GaN wire section proceeds under the injection of trimethylgallium (TMGa), NH_3, and silane at 800 mbar. The growth temperature is set to 1040 °C, and the V/III ratio is maintained at 50. This low V/III ratio combined with silane injection (≈200 nmol/min) enhances the vertical growth rate of the GaN wires and preserves the wire geometry. The n-type carrier concentration of this first segment is around 10^{20} cm^{-3} [23] and its length around 20−25 μm (for 300 s of growth). Then, the silane flux is switched off, and a nonintentionally doped section is subsequently grown. The n-type carrier concentration of this 15−20 μm segment is about 10^{18} cm^{-3} for equivalent growth time.

Two types of active regions were radially grown on the upper part of these GaN wires, as described in Figure 1. These heterostructures were grown at a reduced pressure of 400 mbar under the injection of triethylgallium (TEGa), trimethylindium (TMIn), and ammonia (NH_3). Type-A heterostructure consists of a single InGaN segment

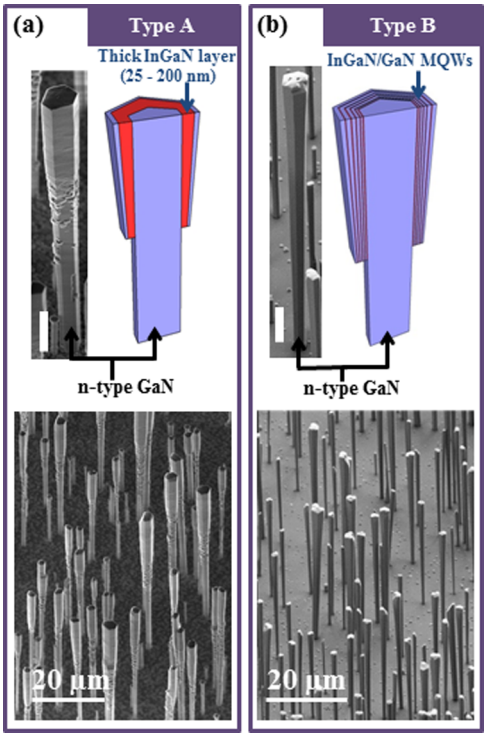

Figure 1. Scanning electron microscopy images (45° tilt) of individual wires and assemblies with their schematics of (a) type A wires, the active region is composed of a single $In_{0.1}Ga_{0.9}N$ layer (25 to 200 nm thickness), and (b) type B wires, the active region consists of 30× $In_{0.18}Ga_{0.82}N$/GaN MQWs. The nonannotated scale bars in the SEM images are 5 μm.

DOI: 10.1021/acsami.5b06473
ACS Appl. Mater. Interfaces 2015, 7, 21898−21906

grown at 750 °C with V/III ratio of ≈6000; its thickness was varied between 25 and 200 nm. For such a thick layer, the indium content target was kept around 10% in order to limit the occurrence of plastic relaxation. Type-B heterostructure is composed of 30 InGaN/GaN MQWs with an In composition target of 18%. The InGaN wells were grown at 720 °C while the nonintentionally doped GaN barriers were grown at 900 °C (V/III ratio of ≈6000). A SiN_x selective growth layer is spontaneously formed at the bottom surface of the wires by providing silane during the growth.[24] This layer may prevent the radial growth, and its efficiency depends on the silane quantity, materials composition, and growth conditions. For type A heterostructure, the shell covers the upper half of the wire length while for type B heterostructure the shell goes down almost to the bottom of the wire.

For both types of active regions (A and B), the final layer of the radial heterostructure is a p-GaN shell (about 300 and 100 nm thick for type A and B heterostructure, respectively) grown at 920 °C in nitrogen (N_2) with biscyclopentadienyl-magnesium precursor (Cp2Mg). Activation of the magnesium dopants was performed at 750 °C for 20 min in N_2 atmosphere. After this annealing process, the acceptor density is estimated to be in the 10^{16}–10^{17} cm^{-3} range. As shown in Figure 1, the as-grown type A and B wires exhibit a similar morphology with a density of about 10^6 cm^{-2}; their diameter in the upper part goes from 700 nm to 1.5 μm.

2.2. Fabrication Process of Photovoltaic Devices. The core–shell GaN/InGaN wires were processed into photovoltaic devices using standard microfabrication techniques. The wires are first removed from their native substrates by sonication in ethanol and dispersed on a SiO_2/Si substrate. Because the wire diameter is in the micrometer range, a planarization step is required to provide a mechanical support for the metallic contacts. The sample is coated with hydrogen silsesquioxane (HSQ) resist that is converted into SiO_x after furnace baking at 400 °C for 1 h. Wet etching in a diluted HF solution (HF/H_2O = 1:200 volume) is then performed to uncover the upper half of the wire.

Electrical contacts are defined on the n- and p-type sections of the wires by optical processes with localized contacts (hereafter, named B-1 and B-3) or by electron beam lithography for extended contacts (named B-2). Examples of processed wires are shown in scanning electron microscopy (SEM) images of Figure 2. Thanks to the micrometer size of the wires, it is possible to deposit localized metal contacts on single wires using optical lithography. A mask with predefined electrode patterns is employed to contact individually selected wires one after another by performing successive exposures. Tens of wires can be contacted in the same run. The use of electron beam lithography is required for the B-2 process because of the specific contact geometry covering the entire core/shell region, for which the precise alignment is critical. The experimental method is described in detail below.

Metal deposition is performed by e-beam evaporation followed by lift-off in acetone. Metallic contact on the n-GaN core consists of Ti/Al/Ti/Au (10/20/10/200 nm). Concerning the p-type contact on the GaN shell, three different processes were carried out on type B wires to study the contact influence on carrier collection and photovoltaic properties (Section 4.2). In the standard process (B-1), the p-type contact is made of Ni/Au (10/200 nm) without an additional annealing step. In the B-2 process, an extended contact is fabricated over the entire p-GaN shell of the wire. The contact is composed of 5 nm-thin Ni layer deposited by e-beam evaporation and 100 nm-thick sputtered indium tin oxide (ITO). The Ni sublayer is employed to reduce the contact resistance on the p-GaN shell.[25] The ITO layer is annealed at 400 °C for 10 min to increase its conductivity. The next step is the deposition of Ti/Al/Ti/Au (10/20/10/200 nm) on the ITO layer for the electrical connection to macroscopic pads by microbonding. The third process (B-3) uses a thin bilayer of Ni/Au (5/5 nm) deposited by e-beam evaporation. This first metal stack is annealed at 500 °C in ambient atmosphere for 5 min to favor the formation of NiO on p-GaN. A second lithography and deposition of Ni/Au (10/200 nm) is performed afterward (see Figure 2).

2.3. STEM Characterization. The wire structural properties were probed by scanning transmission electron microscopy (STEM) using a high-angle annular dark-field (HAADF) detector which provides images whose contrast is directly linked to the number of electrons ($\sim Z^{1.7}$).[26] The samples were prepared in cross sections perpendicular to the growth axis by a focused ion beam (Nvision 40, Carl Zeiss). A tungsten protective layer was first deposited before Ga-thinning the wires at different high voltages (30–5 kV) to reduce ion damage. HAADF images taken along the [0001] zone axis of type A and B wires (see Figure 3) show that both types of wires present well-defined core/shell geometry with InGaN/GaN deposition on the m-plane facets of the $\bar{c}$-axis GaN wires. A good uniformity from facet to facet of the InGaN thickness is observed.

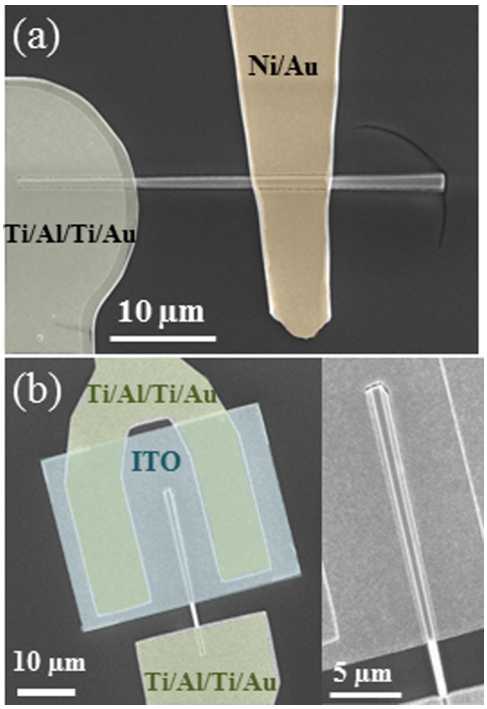

Figure 2. Scanning electron microscopy (SEM) images of contacted type B wires. (a) Process B-1: localized p-type contact made of Ni/Au (5/200 nm). (b) Process B-3: extended p-type contact consisting of annealed Ni/ITO (5/100 nm). The inset of panel (b) shows a higher magnification SEM image of the wire from panel (b).

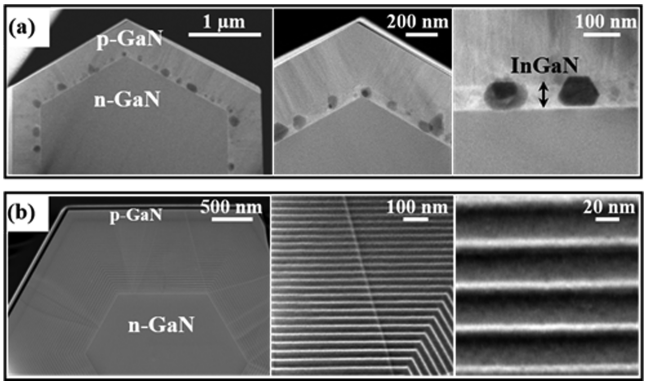

Figure 3. High-angle annular dark-field (HAADF) cross sectional electron microscopy images of (a) a wire with 60 nm $In_{0.1}Ga_{0.9}N$ shell and (b) a wire with 30× $In_{0.18}Ga_{0.82}N$/GaN MQWs shell.

The thick InGaN shell is damaged by a high density of voids (see dark contrast in Figure 3a), not present in the GaN core. These voids generally exhibit well-defined $\{1\bar{1}00\}$ facets, and their size varies from 50 to 200 nm. They often extend beyond the InGaN layer and affect the p-GaN shell. Numerous defects are also present in the p-GaN layer

DOI: 10.1021/acsami.5b06473
ACS Appl. Mater. Interfaces 2015, 7, 21898–21906

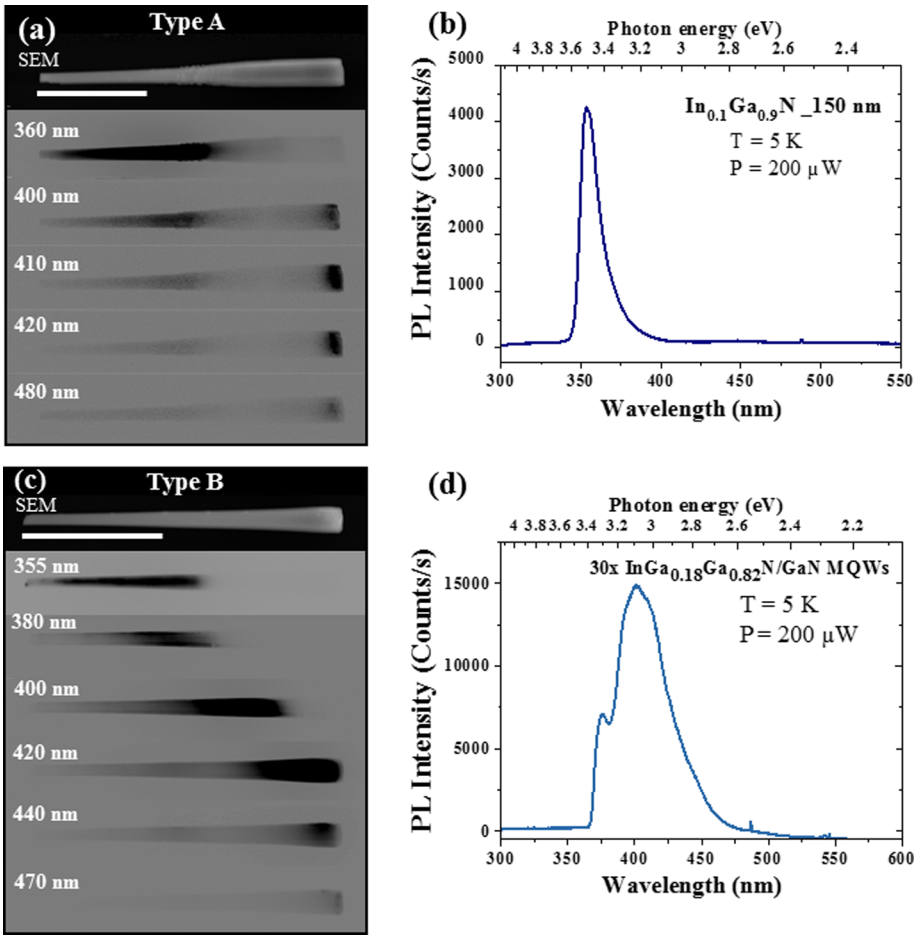

Figure 4. Low-temperature (5 K) cathodoluminescence (CL) and photoluminescence (PL) measurements for type A and B core−shell wires. (a and c) CL mappings on single wires. (b and d) PL spectra on corresponding wire ensembles.

in the form of radial stripes that originate at the InGaN/p-GaN interface, the defect density being reduced in the corner regions of the hexagon.

Similar void structures with defined facets have been reported in $(20\bar{2}1)$ semipolar single QW LED by Zhao et al.[27] In polar c-plane interfaces, Yankovich et al.[28] reported pyramidal voids in $In_{0.08}GaN_{0.92}/In_{0.01}GaN_{0.99}$ MQWs affecting both the InGaN and GaN layers. The formation of such hollow structures was ascribed to carbon deposition; in our case, passivation by residual silicon and surface energy minimization might play the same role.

Type-B wires were analyzed with the same method in Figure 3b. The dark (bright) contrast is associated with the GaN barrier (InGaN well). The quantum well period is about 30.5 nm with a quantum well thickness of 6 nm. In certain areas of the shell, the MQW structure is disturbed by dislocations nucleated at the GaN core/first QW interface and propagating across the heterostructure. Contrary to type A wire, the p-GaN layer is not degraded by defects.

2.4. Cathodoluminescence and Photoluminescence Spectroscopy. The optical properties of single wires were probed by low temperature cathodoluminescence (CL). The CL mapping was performed at 5 K with an electron beam energy of 30 kV. Wire ensembles dispersed on silicon substrate were also probed by photoluminescence (PL) spectroscopy at 5 K using a frequency-doubled continuous wave Ar^{2+} laser emitting at 244 nm (200 μW laser power).

Figure 4a shows a representative illustration of the CL mapping along a wire with a 150 nm-thick InGaN layer. The contribution at 360 nm corresponds to the GaN near band edge emission and is associated with the n-GaN section of the wire.[29] Between 410 and 430 nm, the emission comes preferentially from the top region of the heterostructure. However, this rather weak contribution of the InGaN layer does not appear when probing wire ensembles by PL as shown in Figure 4b. The PL spectrum reveals indeed a single peak at 353 nm with a full width at half-maximum (fwhm) of 15 nm which corresponds to the GaN near band edge emission. This peak exhibits an asymmetric shape with a slight broadening toward longer wavelengths. The absence of a detectable contribution of the InGaN layer in PL is likely related to its poor material quality that has been previously evidenced by TEM.

Contrary to type A wires, the luminescence of type B wires comes from the entire heterostructure region as shown by the CL mappings of Figure 4c. The CL mappings evidence a red shift of the emission wavelength along the wire axis: the luminescence increases from 380 to 420 nm. This red shift is attributed to a gradient of indium composition along the core−shell region with more indium incorporated in the top part of the heterostructure. Luminescence above 450 nm is associated with the axial MQWs grown on the $(000\bar{1})$ top c-facet.[30] This is probably related to the larger In incorporation on c-plane surfaces than on m-plane ones[31] and also to the influence of the spontaneous and piezoelectric fields on polar planes for such thick quantum wells (quantum-confined Stark effect). PL measurement carried out on wire ensembles shown in Figure 4d confirms that the indium incorporation is not homogeneous and presents quite large fluctuations. The PL spectrum shows a broad contribution with a main peak located at 400 nm (fwhm = 45 nm) that extends to 450 nm on the low energy side. The absence of the GaN contribution, evidenced by CL analysis around 355 nm, attests that the carrier capture and the radiative recombination in the MQWs system is efficient. The PL spectrum displays a secondary peak centered at 375 nm which could be attributed to donor−acceptor pair (DAP) recombination in the p-GaN shell.[32]

DOI: 10.1021/acsami.5b06473
ACS Appl. Mater. Interfaces 2015, 7, 21898−21906

3. RESULTS AND DISCUSSION

Photovoltaic properties of individual wires were probed at room temperature using a commercial AAA grade solar simulator calibrated to deliver a power density of 100 mW/cm^2 corresponding to 1 sun AM1.5G illumination. $I-V$ characteristics in the dark and under illumination were measured using a Keithley 2636 source meter. A total of 50 wires were investigated to obtain a statistically representative set of data.

3.1. Active Region Design: Thick InGaN Layers and MQWs. The photovoltaic properties of GaN/InGaN wires were evaluated by comparing two types of active regions. In type A design, the aim was to investigate the improvement of light absorption with increasing InGaN thickness. For this purpose, the InGaN layer thickness was varied between 25 and 200 nm. We assume that photonic effects such as wavelength absorption dependence on the wire geometry observed in core−shell nanowires[33,34] can be neglected in the present case because of the micrometer diameter of the wires exceeding the illumination wavelength by several times, which should lead to a quasi-planar absorption behavior (the validity of this assumption will be addressed in a further work by simulations taking into account the wire's shape and the absorber geometry).

Figure 5a shows the $J-V$ characteristics in the dark and under illumination for wires with a 25 and 150 nm thick

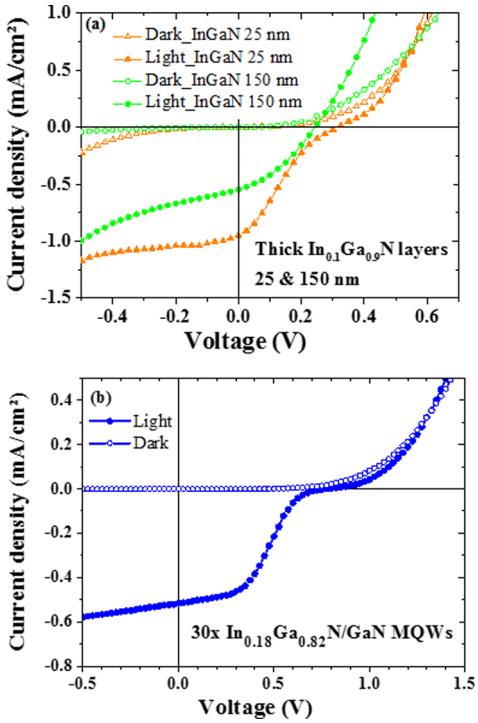

Figure 5. Current density versus voltage characteristics in the dark and under illumination (1 sun, AM1.5G) of single wires with (a) a thick $In_{0.1}Ga_{0.9}$ N segment (25 and 150 nm) and (b) 30× $In_{0.18}Ga_{0.82}N$/GaN MQWs.

$In_{0.1}Ga_{0.9}N$ layer (200 nm thickness exhibiting a similar behavior; 50 and 100 nm giving lower photoresponse). The wire with a 25 nm $In_{0.1}Ga_{0.9}N$ segment has 0.95 mA/cm^2 short-circuit current (J_{sc}) and 0.32 V open circuit voltage (V_{oc}), while J_{sc} = 0.54 mA/cm^2 and V_{oc} = 0.23 V for a 150 nm segment. Wires with a 25 nm $In_{0.1}Ga_{0.9}N$ layer exhibit a rather high J_{sc}; however, increasing the thickness of the InGaN layer to 150 nm did not improve the photoresponse intensity. Concerning the performance in terms of V_{oc}, measured values are very low compared to the ones in the literature in the 1.5−2.3 V range.[2,6] This important reduction in V_{oc} is a signature of the presence of a large amount of nonradiative recombination centers in the InGaN layer as suggested by PL results. This can probably be attributed to voids in the InGaN segment and defects in the p-GaN shell as previously evidenced by TEM observations (see Figure 3) and possibly to indium inhomogeneities in the InGaN layer.[10]

The fill factor (FF) of the devices (ratio between the maximum output power and $J_{sc} \times V_{oc}$) is 22% and 34% for the wires with 25 and 150 nm-thick $In_{0.1}Ga_{0.9}N$ segments, respectively. These low FF values are probably related to the high series and low shunt resistances and to the nonconventional "S-shape" feature of the $J-V$ curves under illumination. R_{series} was estimated to be 200−300 Ω·cm^2 from the comparison between the light and dark $J-V$ curves around the maximum power point following the method described in ref 35, and R_{shunt} is about 700−800 Ω·cm^2 from the $I-V$ curve fitting near J_{sc}. The S-shape behavior is illustrated in Figure 5a by the $J-V$ curve of the 25 nm-thick wire, where an inflection point is observed around 0.1 V (and more generally between −0.5 and 0.5 V considering a sampling of 26 wires). The photocurrent decreases dramatically from this inflection point. Such an S-shaped feature reduces the squareness of the illuminated $J-V$ curve and therefore reduces the fill factor. Its nature will be discussed in the following paragraphs.

For the type B active region, $InGaN_{0.18}/Ga_{0.82}N$ MQWs improve the crystalline quality of the core−shell heterostructure, as already demonstrated by the optimization of planar InGaN/GaN MQWs solar cells grown in the same setup.[6,36] Figure 5b shows its $J-V$ characteristics in the dark and under illumination. This second design improves the wire performances, in particular the V_{oc} and FF values. The best wire gives J_{sc} = 0.52 mA/cm^2, V_{oc} = 0.58 V, and FF = 51% resulting in a conversion efficiency of $\eta = 0.19 \pm 0.02\%$. However, the $J-V$ curve under illumination of the device is still affected by an S-shape behavior around V = 0.5 V reducing the fill factor.

A similar S-shape feature has been reported previously by Neufeld et al.[37] for planar InGaN solar cells, who proposed that polarization charges at the InGaN/GaN c-plane interface are at the origin of the kink in the light $J-V$ curve. These charges induce an electric field in the active region, which hinders the diffusion of photogenerated carriers toward the contacts. In our case, the MQWs are grown on the nonpolar m-plane $\{10\bar{1}0\}$ facets of the c-oriented GaN wires, which are not affected by the internal electric field; consequently, the explanation by Neufeld et al.[37] does not apply here.

Reports on organic solar cells have also shown this type of behavior.[38] The common explanation is the presence of a potential barrier at the interface between the active region and the electrode that prevents the extraction of electrons (or holes) at the cathode (or anode). The consequence is a reduction of the forward current together with a deformation of the illuminated $J-V$ curve.[39] The main reasons of the existence of an extraction barrier include nonohmic contacts[40] and segregation or impurities in the active region.[41,42] In our case, it is likely that this effect arises from the nonohmic nature of the Ni/Au contact on the p-GaN shell. The electric field at the metal/p-GaN interface is in the opposite direction to the built-in electric field of the p−n junction and thus induces a potential

DOI: 10.1021/acsami.5b06473
ACS Appl. Mater. Interfaces 2015, 7, 21898−21906

barrier for carrier collection. The presence of a Schottky barrier in nonannealed Ni/Au contacts to p-doped GaN wire shell has been previously evidenced in a similar structure using electron beam induced current (EBIC) microscopy.[43] The realization of an ohmic contact on p-type GaN is challenging because of the difficulty to reach a high doping level in p-type GaN layers and the absence of metals with a workfunction equal to 7.5 eV (sum of the GaN bandgap and electron affinity energy). To address this issue, different strategies have been developed and the lowest contact resistances have been obtained by the deposition of a thin bilayer of Ni/Au followed by a high temperature annealing step (400−500 °C) in oxidizing ambient to form NiO. It has indeed been reported that the use of NiO helps in decreasing the specific contact resistance on p-GaN by 2 orders of magnitude.[44]

3.2. P-Type Contact Optimization. Carrier collection plays a major role in solar cell operation and as a consequence contacts need to be carefully designed in order to avoid losses. The previously described p-contact design, based on nonannealed Ni/Au stripes (B-1 process), presents two main drawbacks. As mentioned before, the S-shape photocurrent decrease can be related to the nonohmic nature of the p-type contact and carrier losses could also occur during transport along the p-GaN shell. This has been evidenced by EBIC measurements[43] on similar wires: carriers generated far away from the contact are poorly collected by the p-type electrode because of a high resistance of the p-GaN shell. EBIC measurements described in Section 4.1 confirm this effect. In order to further investigate the influence of the p-type contact on the wire photovoltaic properties, two strategies were implemented on type B heterostructures (wires with 30 MQWs).

In the first approach (process B-2), the goal was to realize a transparent Ni/ITO contact covering the p-GaN shell to improve the carrier collection along the shell. In the second approach (process B-3), the aim was to reduce the Schottky barrier at the metal/p-GaN interface by annealing the Ni/Au bilayer in oxidizing atmosphere to form NiO. The realization of the n-type contact remained the same as described above in the Experimental Methods. The PV performances of wires processed according to these procedures are summarized in Table 1.

Table 1. Summary of the MQW Device Performances under 1 sun Illumination (AM1.5G)[a]

contact	J_{sc} (mA/cm^2)	V_{oc} (V)	FF (%)	η (%)
B-1: Ni/Au	0.38 ± 0.19	0.62 ± 0.24	24 ± 18	0.085 ± 0.084
B-2: Ni/ITO annealed	0.26 ± 0.03	0.68 ± 0.09	55 ± 6	0.10 ± 0.03
B-3: Ni/Au annealed	0.55 ± 0.11	0.72 ± 0.14	64 ± 9	0.25 ± 0.07

[a]Average and standard deviation values were calculated from measurements on 6 to 8 wires for each processing type.

Figure 6 displays the $J-V$ curves in the dark and under illumination of a wire processed with a Ni/ITO contact. This wire exhibits the best performance of this series with FF = 66% and η = 0.15 ± 0.01%. The presented illuminated $J-V$ curve is not deformed, which is the case for half of the measured wires (4 over 8). For the other half, the light $J-V$ curve presents an S-shape, but the kink is less pronounced than for wires with nonannealed Ni/Au contacts. An average FF of 55% and η of

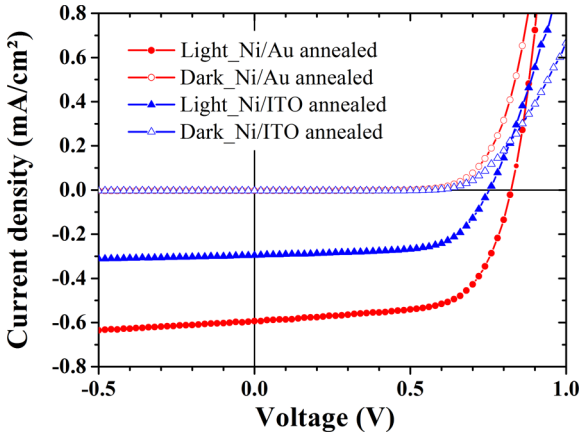

Figure 6. Current density versus voltage characteristics under 1 sun (AM1.5G) of 30× $In_{0.18}Ga_{0.82}N$/GaN MQW wires with annealed Ni/Au and Ni/ITO contacts.

0.10 ± 0.01% were obtained over 8 wires. A slight improvement is observed concerning the V_{oc} with an average value of 0.68 V (instead of 0.62 V for nonannealed Ni/Au contacts). However, the performance in terms of J_{sc} is quite modest with an average value of 0.26 mA/cm^2, despite the use of an extended contact covering the entire core/shell region. This systematic current decrease could be related to carrier absorption by the ITO and/or Ni layer. Reducing the layer thickness and exploring alternative transparent contact materials such as graphene[45] will be attempted in our following investigations to minimize carrier losses by absorption. Figure 6 shows the $J-V$ curves in the dark and under illumination of wires with annealed Ni/Au contacts. The first notable feature is the complete suppression of the S-shape behavior in the $J-V$ characteristics under illumination. No S-shape feature has been observed for any of 8 studied wires. The absence of inflection point results in higher FF values and improved conversion efficiencies as compared to wires with nonannealed Ni/Au contacts. The average FF has increased from 24% to 64%; likewise, the average conversion efficiency shows drastic improvement with a 3-fold increase (from 0.085% to 0.25%). A fill factor of 83% and a conversion efficiency of 0.33 ± 0.02% were obtained for the best device. On average (measurements performed over 8 wires), we also observed a 16% increase in V_{oc} (the best value being 0.95 V) and a 44% increase in J_{sc} (maximum value: 0.60 mA/cm^2). Overall, devices with annealed contacts exhibited more homogeneous characteristics as shown in Table 1 by the reduced standard deviation of the measurements. These performances are also reproducible as no variation in the $I-V$ curves could be observed after running the same measurement several times. In spite of the contact optimization, the average V_{oc} remained low, which means that further improvement of the structure is still required to reduce the amount of recombination. It has indeed been reported in planar InGaN solar cells that thick InGaN QWs (t > 3 nm) exhibit a higher defect density that can be directly related to lower V_{oc} values.[36] Comparison of the three p-type contact designs shows a clear benefit for wires processed with annealed Ni/Au contacts.

4. ADVANCED ELECTRICAL CHARACTERIZATION

4.1. Electron Beam Induced Current Microscopy. The spatial distribution of the current generation in wires with annealed Ni/Au contacts has been studied by electron beam

DOI: 10.1021/acsami.5b06473
ACS Appl. Mater. Interfaces 2015, 7, 21898−21906

induced current microscopy. The EBIC microscopy consists of a local generation of electron−hole pairs by the electron beam. The presence of a built-in field in the core/shell p−n junction induces electron−hole pair separation and produces a current signal.[46] The EBIC maps of the contacted wires were measured at room temperature in a Hitachi SU8000 SEM by scanning the device surface with an electron beam at normal incidence to the substrate. The metallic pads were contacted using micromanipulators connected to a Stanford Research System SR570 low-noise current preamplifier. Further details about the EBIC setup can be found in refs 43 and 47. No external bias was applied to the wire. The electron beam acceleration voltage and the extraction current were set, respectively, to 10 kV and 10 μA leading to a 0.44 nA beam current impinging the sample surface.

Figure 7a,b shows a SEM image and a corresponding EBIC map of a representative type B wire. As seen from the EBIC

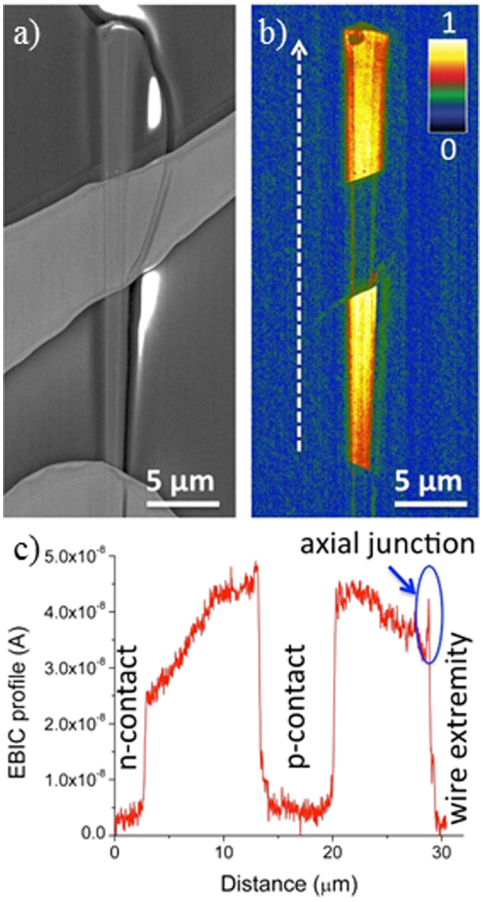

Figure 7. (a) SEM image and (b) the corresponding normalized EBIC map of a contacted type B wire with annealed Ni/Au p-contact. The dashed arrow shows the direction of the EBIC profile in panel (c). (c) EBIC profile along the wire axis.

map, the device generates current over the entire core/shell region in accordance with the radial p−n junction. However, as seen from the EBIC profile along the wire axis shown in Figure 7c, the magnitude of the EBIC current is reduced for excitation positions located far from the p-contact (e.g., a signal drop of 25% is observed 10 μm away from the p-contact toward the wire top). This effect has previously been observed in similar core/shell GaN/InGaN wires and has been attributed to significant p-GaN shell resistance, which prevents efficient collection of holes generated far from the p-contact.[43] This observation demonstrates that the collection efficiency can be further improved by implementing an extended contact over the entire core/shell region with a good transparency to avoid parasitic absorption. Separate EBIC mappings at low acceleration voltage of 3 kV have not shown any signature of Schottky barrier close to the p-contact contrary to previous experiments with nonannealed Ni/Au contacts.[43] A narrow peak in the EBIC profile is systematically observed at the wire top extremity. It is attributed to the contribution of the axial p−n junction. A stronger EBIC signal from this region is due to a simultaneous excitation of the radial and axial p−n junctions when the beam approaches the wire top extremity.

4.2. Photocurrent Spectroscopy. The spectral dependence of the PV conversion was probed by means of photocurrent spectroscopy for type B wires with extended Ni/ITO contact (B-2) and annealed Ni/Au stripes (B-3). The measurement was performed using a tunable visible-UV light source consisting of a Xe lamp coupled with a Jobin Yvon Triax 180 spectrometer. The light was mechanically chopped at 4 Hz, and the signal was demodulated using a lock-in detector. The measurement was carried out in short-circuit conditions under zero bias. Figure 8 compares typical photocurrent spectra of B-

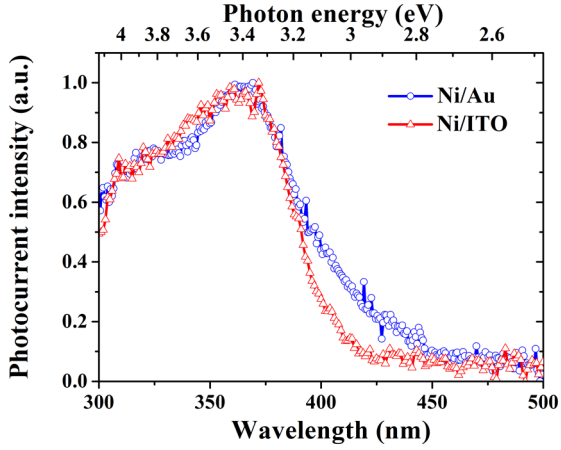

Figure 8. Photocurrent spectra of 30× $In_{0.18}GaN_{0.82}$/GaN MQW wires with extended Ni/ITO contact (B-2) and annealed Ni/Au stripes (B-3).

2 and B-3 wires. Starting from the UV range (300 nm), the photocurrent increases to reach its maximum value around 360 nm for both types of wires before decreasing for longer wavelengths. For ITO-covered B-2 wires, the slope is steep from 300 to 310 nm reflecting the ITO absorption at short wavelengths. B-2 and B-3 wires exhibit similar photoresponse with slightly different long wavelength tails extending to 420 and 440 nm, respectively. This insignificant cutoff difference on the long wavelength side is most probably related to compositional wire-to-wire fluctuations and not to the contact layout.

A significant spectral shift is observed between the photocurrent response and the CL emission of the MQW wires. Although a strong CL signal was observed at 400−420 nm wavelengths, the wire photoresponse is weak in this spectral range. This can be explained by the reduction of the carrier extraction efficiency with increasing In-content in the QWs. Indeed, carriers excited in the In-rich regions of the QW can efficiently contribute to the CL signal; however, the extraction

DOI: 10.1021/acsami.5b06473
ACS Appl. Mater. Interfaces 2015, 7, 21898−21906

efficiency assisted by thermal excitation decreases exponentially with the QW depth and becomes very weak. We note that, within the experimental accuracy, the photocurrent spectra do not show any contribution from the axial QWs (expected at wavelength above 450 nm based on CL measurements). This is due to the above-mentioned low carrier extraction from In-rich QWs. The issue of low carrier extraction could be addressed by decreasing the barrier thickness in order to increase carrier extraction by the tunneling mechanism.[48,49] As shown by Redaelli et al.,[49] solar cells based on a MQWs system with thin barriers (~3.7 nm) exhibit higher external quantum efficiency than their thick barriers counterparts. By thinning the barrier thickness, the total thickness of the active region will be reduced and the effective electric field of the p−n junction will be increased. Its magnitude can be also optimized by enhancing the doping of the n- and most importantly of the p-type regions. More generally, the MQW approach for InGaN solar cells requires a balance between In-content, well, and barrier thicknesses to get an optimization of the collection electric field as well as a pseudomorphic growth preventing defect formation and localization effect.

5. CONCLUSION

We have investigated the photovoltaic properties of core−shell InGaN/GaN wires. Two types of active region designs were explored: thick $In_{0.1}Ga_{0.9}N$ layers and $In_{0.18}Ga_{0.82}N$/GaN MQWs. The MQW design showed superior photovoltaic performances due to improved structural properties. Optimization of the contact on the p-GaN shell allowed one to suppress the S-shape behavior affecting the illuminated $J-V$ characteristics and resulted in higher fill factor and conversion efficiencies. Best performances were obtained with Ni/Au annealed contacts. A conversion efficiency of 0.33% together with a fill factor of 83% was reached on a 30× $In_{0.18}Ga_{0.82}N$/GaN wire under 1 sun illumination (AM1.5G). The photovoltaic response is restricted to wavelengths below 440 nm. Future strategies to increase the conversion efficiency include the improvement of the crystalline quality of the active region and the passivation of the wire surface by a high bandgap semiconductor (AlGaN) to reduce the surface recombination.

AUTHOR INFORMATION

Corresponding Authors

*E-mail: Agnes.Messanvi@cea.fr.
*E-mail: Maria.Tchernycheva@u-psud.fr.

Notes

The authors declare no competing financial interest.

ACKNOWLEDGMENTS

C.D, J.E., M.T., and M.F. have been financially supported by ANR-14-CE26-0020-01 project PLATOFIL. A.M. has been financially supported by Laboratory of Excellence 'GaNeX' (ANR-11-LABX-2014). IEF team (M.T., H.Z., V.N., F.H.J., and F.B.) has been supported by ANR program 'NanoSaclay' (ANR-10-LABX-0035) and by FP7 Marie Curie projects 'Funprob' and 'NanoEmbrace' (grant no. 316751). A.B. acknowledges the support of RFBR (Project Nos. 15-02-08282 A and 14-02-31485) and of the Scholarship of the President of the Russian Federation for young scientists and graduate students (Grant No. SP-4716.2015.1). The device processing has been performed at CTU-IEF-Minerve technological platform, member of the Renatech RTB network. We thank Jean-René Coudevylle (CTU-IEF-Minerve) for support in the fabrication process and Jean Dussaud (Néel Institute) for the MOCVD technical support as well as Fabrice Donatini (Néel Institute) and Matthias Belloeil (CEA-INAC) for help in CL and PL measurements, respectively.

REFERENCES

(1) Wu, J.; Walukiewicz, W.; Yu, K. M.; Ager, J. W.; Haller, E. E.; Lu, H.; Schaff, W. J. Small Band Gap Bowing in $In_{1-x}Ga_xN$ Alloys. *Appl. Phys. Lett.* **2002**, *80*, 4741.
(2) Farrell, R. M.; Neufeld, C. J.; Cruz, S. C.; Lang, J. R.; Iza, M.; Keller, S.; Nakamura, S.; DenBaars, S. P.; Mishra, U. K.; Speck, J. S. High Quantum Efficiency InGaN/GaN Multiple Quantum Well Solar Cells with Spectral Response Extending out to 520 Nm. *Appl. Phys. Lett.* **2011**, *98*, 201107.
(3) Wu, J.; Walukiewicz, W.; Yu, K. M.; Shan, W.; Ager, J. W.; Haller, E. E.; Lu, H.; Schaff, W. J.; Metzger, W. K.; Kurtz, S. Superior Radiation Resistance of $In_{1-x}Ga_xN$ Alloys: Full-Solar-Spectrum Photovoltaic Material System. *J. Appl. Phys.* **2003**, *94*, 6477.
(4) Mori, M.; Kondo, S.; Yamamoto, S.; Nakao, T.; Iwaya, M.; Takeuchi, T.; Kamiyama, S.; Akasaki, I.; Amano, H. Concentrating Properties of Nitride-Based Solar Cells Using Different Electrodes. *Jpn. J. Appl. Phys.* **2013**, *52*, 08JH02.
(5) Dahal, R.; Li, J.; Aryal, K.; Lin, J. Y.; Jiang, H. X. InGaN/GaN Multiple Quantum Well Concentrator Solar Cells. *Appl. Phys. Lett.* **2010**, *97*, 073115.
(6) Valdueza-Felip, S.; Mukhtarova, A.; Grenet, L.; Bougerol, C.; Durand, C.; Eymery, J.; Monroy, E. Improved Conversion Efficiency of as-Grown InGaN/GaN Quantum-Well Solar Cells for Hybrid Integration. *Appl. Phys. Express* **2014**, *7*, 032301.
(7) Holec, D.; Zhang, Y.; Rao, D. V. S.; Kappers, M. J.; McAleese, C.; Humphreys, C. J. Equilibrium Critical Thickness for Misfit Dislocations in III-Nitrides. *J. Appl. Phys.* **2008**, *104*, 123514.
(8) Ho, I.-H.; Stringfellow, G. B. Solid Phase Immiscibility in GaInN. *Appl. Phys. Lett.* **1996**, *69*, 2701−2703.
(9) Kuwahara, Y.; Fujii, T.; Sugiyama, T.; Iida, D.; Isobe, Y.; Fujiyama, Y.; Morita, Y.; Iwaya, M.; Takeuchi, T.; Kamiyama, S.; Akasaki, I.; Amano, H. GaInN-Based Solar Cells Using Strained-Layer GaInN/GaInN Superlattice Active Layer on a Freestanding GaN Substrate. *Appl. Phys. Express* **2011**, *4*, 021001.
(10) Bhuiyan, A. G.; Sugita, K.; Hashimoto, A.; Yamamoto, A. InGaN Solar Cells: Present State of the Art and Important Challenges. *IEEE J. Photovoltaics* **2012**, *2*, 276−293.
(11) Coulon, P. M.; Mexis, M.; Teisseire, M.; Jublot, M.; Vennéguès, P.; Leroux, M.; Zuniga-Perez, J. Dual-Polarity GaN Micropillars Grown by Metalorganic Vapour Phase Epitaxy: Cross-Correlation between Structural and Optical Properties. *J. Appl. Phys.* **2014**, *115*, 153504.
(12) Kishino, K.; Ishizawa, S. Selective-Area Growth of GaN Nanocolumns on Si(111) Substrates for Application to Nanocolumn Emitters with Systematic Analysis of Dislocation Filtering Effect of Nanocolumns. *Nanotechnology* **2015**, *26*, 225602.
(13) Hersee, S. D.; Sun, X.; Wang, X. The Controlled Growth of GaN Nanowires. *Nano Lett.* **2006**, *6*, 1808−1811.
(14) Wang, X.; Hartmann, J.; Mandl, M.; Sadat Mohajerani, M.; Wehmann, H.-H.; Strassburg, M.; Waag, A. Growth Kinetics and Mass Transport Mechanisms of GaN Columns by Selective Area Metal Organic Vapor Phase Epitaxy. *J. Appl. Phys.* **2014**, *115*, 163104.
(15) Wallentin, J.; Anttu, N.; Asoli, D.; Huffman, M.; Aberg, I.; Magnusson, M. H.; Siefer, G.; Fuss-Kailuweit, P.; Dimroth, F.; Witzigmann, B.; Xu, H. Q.; Samuelson, L.; Deppert, K.; Borgstrom, M. T. InP Nanowire Array Solar Cells Achieving 13.8% Efficiency by Exceeding the Ray Optics Limit. *Science* **2013**, *339*, 1057−1060.
(16) Catchpole, K. R.; Mokkapati, S.; Beck, F.; Wang, E.-C.; McKinley, A.; Basch, A.; Lee, J. Plasmonics and Nanophotonics for Photovoltaics. *MRS Bull.* **2011**, *36*, 461−467.

DOI: 10.1021/acsami.5b06473
ACS Appl. Mater. Interfaces 2015, 7, 21898−21906

(17) Wierer, J. J., Jr.; Li, Q.; Koleske, D. D.; Lee, S. R.; Wang, G. T. III-Nitride Core−shell Nanowire Arrayed Solar Cells. *Nanotechnology* **2012**, *23*, 194007.
(18) Cansizoglu, M. F.; Hamad, S. M.; Norman, D. P.; Keles, F.; Badraddin, E.; Karabacak, T.; Seo, H. PiN InGaN Nanorod Solar Cells with High Short-Circuit Current. *Appl. Phys. Express* **2015**, *8*, 042302.
(19) Young, N. G.; Farrell, R. M.; Hu, Y. L.; Terao, Y.; Iza, M.; Keller, S.; DenBaars, S. P.; Nakamura, S.; Speck, J. S. High Performance Thin Quantum Barrier InGaN/GaN Solar Cells on Sapphire and Bulk (0001) GaN Substrates. *Appl. Phys. Lett.* **2013**, *103*, 173903.
(20) Young, N. G.; Perl, E. E.; Farrell, R. M.; Iza, M.; Keller, S.; Bowers, J. E.; Nakamura, S.; DenBaars, S. P.; Speck, J. S. High-Performance Broadband Optical Coatings on InGaN/GaN Solar Cells for Multijunction Device Integration. *Appl. Phys. Lett.* **2014**, *104*, 163902.
(21) Dong, Y.; Tian, B.; Kempa, T. J.; Lieber, C. M. Coaxial Group III−Nitride Nanowire Photovoltaics. *Nano Lett.* **2009**, *9*, 2183−2187.
(22) Koester, R.; Hwang, J. S.; Durand, C.; Le Si Dang, D.; Eymery, J. Self-Assembled Growth of Catalyst-Free GaN Wires by Metal−organic Vapour Phase Epitaxy. *Nanotechnology* **2010**, *21*, 015602.
(23) Tchoulfian, P.; Donatini, F.; Levy, F.; Amstatt, B.; Ferret, P.; Pernot, J. High Conductivity in Si-Doped GaN Wires. *Appl. Phys. Lett.* **2013**, *102*, 122116.
(24) Eymery, J.; Salomon, D.; Chen, X.; Durand, C. Process for Catalyst-Free Selective Growth on a Semiconductor Structure. Patent WO2012136665, 2012.
(25) Lin, Y. C.; Chang, S. J.; Su, Y. K.; Tsai, T. Y.; Chang, C. S.; Shei, S. C.; Kuo, C. W.; Chen, S. C. InGaN/GaN Light Emitting Diodes with Ni/Au, Ni/ITO and ITO P-Type Contacts. *Solid-State Electron.* **2003**, *47*, 849−853.
(26) Pennycook, S. J. Z-Contrast Stem for Materials Science. *Ultramicroscopy* **1989**, *30*, 58−69.
(27) Zhao, Y.; Wu, F.; Huang, C.-Y.; Kawaguchi, Y.; Tanaka, S.; Fujito, K.; Speck, J. S.; DenBaars, S. P.; Nakamura, S. Suppressing Void Defects in Long Wavelength Semipolar (2021) InGaN Quantum Wells by Growth Rate Optimization. *Appl. Phys. Lett.* **2013**, *102*, 091905.
(28) Yankovich, A. B.; Kvit, A. V.; Li, X.; Zhang, F.; Avrutin, V.; Liu, H. Y.; Izyumskaya, N.; Özgür, U.; Morkoç, H.; Voyles, P. M. Hexagonal-Based Pyramid Void Defects in GaN and InGaN. *J. Appl. Phys.* **2012**, *111*, 023517.
(29) Koester, R.; Hwang, J.-S.; Salomon, D.; Chen, X.; Bougerol, C.; Barnes, J.-P.; Dang, D. L. S.; Rigutti, L.; de Luna Bugallo, A.; Jacopin, G.; Tchernycheva, M.; Durand, C.; Eymery, J. M-Plane Core−Shell InGaN/GaN Multiple-Quantum-Wells on GaN Wires for Electroluminescent Devices. *Nano Lett.* **2011**, *11*, 4839−4845.
(30) Jacopin, G.; De Luna Bugallo, A.; Lavenus, P.; Rigutti, L.; Julien, F. H.; Zagonel, L. F.; Kociak, M.; Durand, C.; Salomon, D.; Chen, X. J.; Eymery, J.; Tchernycheva, M. Single-Wire Light-Emitting Diodes Based on GaN Wires Containing Both Polar and Nonpolar InGaN/GaN Quantum Wells. *Appl. Phys. Express* **2012**, *5*, 014101.
(31) Hong, Y. J.; Lee, C.-H.; Yoon, A.; Kim, M.; Seong, H.-K.; Chung, H. J.; Sone, C.; Park, Y. J.; Yi, G.-C. Visible-Color-Tunable Light-Emitting Diodes. *Adv. Mater.* **2011**, *23*, 3284−3288.
(32) Reshchikov, M. A.; Morkoç, H. Luminescence Properties of Defects in GaN. *J. Appl. Phys.* **2005**, *97*, 061301.
(33) Krogstrup, P.; Jørgensen, H. I.; Heiss, M.; Demichel, O.; Holm, J. V.; Aagesen, M.; Nygard, J.; Fontcuberta i Morral, A. *Nat. Photonics* **2013**, *7*, 306.
(34) Amaduzzi, F.; Alarcón-Lladó, E.; Russo-Averchi, E.; Matteini, F.; Heiss, M.; Tütüncüoglu, G.; Conesa-Boj, S.; de la Mata, M.; Arbiol, J.; Fontcuberta i Morral, A. *J. Appl. Phys.* **2014**, *116*, 184303.
(35) Pysch, D.; Mette, A.; Glunz, S. W. A Review and Comparison of Different Methods to Determine the Series Resistance of Solar Cells. *Sol. Energy Mater. Sol. Cells* **2007**, *91*, 1698−1706.
(36) Redaelli, L.; Mukhtarova, A.; Valdueza-Felip, S.; Ajay, A.; Bougerol, C.; Himwas, C.; Faure-Vincent, J.; Durand, C.; Eymery, J.; Monroy, E. Effect of the Quantum Well Thickness on the Performance of InGaN Photovoltaic Cells. *Appl. Phys. Lett.* **2014**, *105*, 131105.
(37) Neufeld, C. J.; Cruz, S. C.; Farrell, R. M.; Iza, M.; Lang, J. R.; Keller, S.; Nakamura, S.; Denbaars, S. P.; Speck, J. S.; Mishra, U. K. Effect of Doping and Polarization on Carrier Collection in InGaN Quantum Well Solar Cells. *Appl. Phys. Lett.* **2011**, *98*, 243507.
(38) Singh, V. P.; Singh, R. S.; Parthasarathy, B.; Aguilera, A.; Anthony, J.; Payne, M. Copper-Phthalocyanine-Based Organic Solar Cells with High Open-Circuit Voltage. *Appl. Phys. Lett.* **2005**, *86*, 082106.
(39) Finck, B. Y.; Schwartz, B. J. Understanding the Origin of the S-Curve in Conjugated Polymer/fullerene Photovoltaics from Drift-Diffusion Simulations. *Appl. Phys. Lett.* **2013**, *103*, 053306.
(40) Gupta, D.; Bag, M.; Narayan, K. S. Correlating Reduced Fill Factor in Polymer Solar Cells to Contact Effects. *Appl. Phys. Lett.* **2008**, *92*, 093301.
(41) Tremolet de Villers, B.; Tassone, C. J.; Tolbert, S. H.; Schwartz, B. J. Improving the Reproducibility of P3HT:PCBM Solar Cells by Controlling the PCBM/Cathode Interface. *J. Phys. Chem. C* **2009**, *113*, 18978−18982.
(42) Wagner, J.; Gruber, M.; Wilke, A.; Tanaka, Y.; Topczak, K.; Steindamm, A.; Hörmann, U.; Opitz, A.; Nakayama, Y.; Ishii, H.; Pflaum, J.; Koch, N.; Brütting, W. Identification of Different Origins for S-Shaped Current Voltage Characteristics in Planar Heterojunction Organic Solar Cells. *J. Appl. Phys.* **2012**, *111*, 054509.
(43) Lavenus, P.; Messanvi, A.; Rigutti, L.; De Luna Bugallo, A.; Zhang, H.; Bayle, F.; Julien, F. H.; Eymery, J.; Durand, C.; Tchernycheva, M. Experimental and Theoretical Analysis of Transport Properties of Core−shell Wire Light Emitting Diodes Probed by Electron Beam Induced Current Microscopy. *Nanotechnology* **2014**, *25*, 255201.
(44) Ho, J.-K.; Jong, C.-S.; Chiu, C. C.; Huang, C.-N.; Shih, K.-K.; Chen, L.-C.; Chen, F.-R.; Kai, J.-J. Low-Resistance Ohmic Contacts to P-Type GaN Achieved by the Oxidation of Ni/Au Films. *J. Appl. Phys.* **1999**, *86*, 4491−4497.
(45) Tchernycheva, M.; Lavenus, P.; Zhang, H.; Babichev, A. V.; Jacopin, G.; Shahmohammadi, M.; Julien, F. H.; Ciechonski, R.; Vescovi, G.; Kryliouk, O. InGaN/GaN Core−Shell Single Nanowire Light Emitting Diodes with Graphene-Based P-Contact. *Nano Lett.* **2014**, *14*, 2456−2465.
(46) Leamy, H. J. Charge Collection Scanning Electron Microscopy. *J. Appl. Phys.* **1982**, *53*, R51−R80.
(47) Tchernycheva, M.; Neplokh, V.; Zhang, H.; Lavenus, P.; Rigutti, L.; Bayle, F.; Julien, F. H.; Babichev, A.; Jacopin, G.; Largeau, L.; Ciechonski, R.; Vescovi, G.; Kryliouk, O. Core−shell InGaN/GaN Nanowire Light Emitting Diodes Analyzed by Electron Beam Induced Current Microscopy and Cathodoluminescence Mapping. *Nanoscale* **2015**, *7*, 11692−11701.
(48) Lang, J. R.; Young, N. G.; Farrell, R. M.; Wu, Y.-R.; Speck, J. S. Carrier Escape Mechanism Dependence on Barrier Thickness and Temperature in InGaN Quantum Well Solar Cells. *Appl. Phys. Lett.* **2012**, *101*, 181105.
(49) Redaelli, L.; Mukhtarova, A.; Ajay, A.; Núñez-Cascajero, A.; Valdueza-Felip, S.; Bleuse, J.; Durand, C.; Eymery, J.; Monroy, E. Effect of the Barrier Thickness on the Performance of Multiple-Quantum-Well InGaN Photovoltaic Cells. *Jpn. J. Appl. Phys.* **2015**, *54*, 072302.

DOI: 10.1021/acsami.5b06473
ACS Appl. Mater. Interfaces 2015, 7, 21898−21906